Imaging of nanoscale charge transport in bulk heterojunction solar cells

Behrang H. Hamadani[a,b], Nadine Gergel-Hackett[c], Paul Haney[a] and Nikolai B. Zhitenev[a,b]
[a] *Center for Nanoscale Science and Technology, National Institute of Standards and Technology, Gaithersburg, MD, 20899 (USA),* [c] *Semiconductor Electronics Division, National Institute of Standards and Technology, Gaithersburg, MD, 20899 (USA)*

We have studied the local charge transport properties of organic bulk heterojunction solar cells based on the blends of poly(3-hexylthiophene) (P3HT) and phenyl-C61-butyric acid methyl ester (PCBM) with a photoconductive atomic force microscope (PCAFM). We explore the role of morphology on transport of photogenerated electrons or holes by careful consideration of the sample geometry and the choice of the atomic force microscope (AFM) tip. We then consider the role of the film/tip contact on the local current-voltage characteristics of these structures and present a model based on a drift and diffusion description of transport. We find that our simple 1D model can only reproduce qualitative features of the data using unphysical parameters, indicating that more sophisticated modeling is required to capture all the nonideal characteristics of the AFM transport measurements. Our results show that the PCAFM contrast can be directly related to the material nanomorphology only under a narrow and well-defined range of the measurement conditions.

[b] Authors to whom correspondence should be addressed.
Electronic mail: behrang.hamadani@nist.gov
Electronic mail: nikolai.zhitenev@nist.gov

Charge transport in blended organic bulk heterojunction (BHJ) solar cells is strongly influenced by the nanoscale morphology and materials self-organization of the donor and acceptor networks.[1-6] The morphology is often crucially dependent on the processing conditions such as the heat and solvent annealing, and the improvement in device performance is generally associated with optimal phase segregation, both in-plane and in the vertical direction[7-9], higher degree of crystallinity, and enhanced charge carrier mobility.[1-4]

One useful technique to investigate the role of nanomorphology of the active layer on charge transport and device efficiency in BHJs is photoconductive atomic force microscopy (PCAFM). In this technique, a conductive atomic force microscope (AFM) tip, replacing the top contact in the solar cell architecture, is raster-scanned on the surface of the film under light excitation, leading to sub-100 nm spatially resolved mapping of the surface photocurrent.[10-14] A complementary measurement is of the dark transport (i.e., current-voltage relation) with a bias voltage applied between the bottom contact (typically an indium tin oxide (ITO) film) and the tip, where the observed contrast is used to extract information regarding the film morphology and composition.[15,16]

Although conductive and photoconductive AFM are powerful nanoscale characterization techniques, understanding and interpreting their results is not straightforward. First, the surface contrast might not be representative of the bulk morphology. For example, in high performance poly(3-hexylthiophene):phenyl-C61-butyric acid methyl ester (P3HT:PCBM) devices where the organic photovoltaic (OPV) layer is deposited on Poly(3,4-ethylenedioxythiophene) poly(styrenesulfonate) (PEDOT:PSS)-coated ITO substrates, a thin layer of P3HT migrates to the free (air) interface[8,9,12] during the film deposition. In PCAFM studies of normal device geometries where electron current is extracted at the top surface, the excess P3HT skin layer forms a barrier layer for electron collection from PCBM crystallites in the bulk, impeding the analysis of the bulk film morphology based on the photocurrent response.[12] Even more problematic, the properties of the microscopic contact between the tip

and the OPV layer, particularly the electrical coupling to electron- and hole-conducting networks as a function of applied bias, are poorly known.

In this work, we analyze the nature of PCAFM contrast exploiting our knowledge of the vertical phase segregation and the top surface nanomorphology of P3HT:PCBM devices[12] thus eliminating most of the uncertainties at the sample surface. Maps of nanoscale photocurrent are measured on both normal and inverted devices using AFM tips with work function suitable for the collection of the appropriate charge (i.e., electrons vs. holes). We then explore the role of the film/tip contact on the local current-voltage (*I-V*) characteristics of these structures and present a physical model devised to reproduce the qualitative features of the data. Our results show that the PCAFM contrast can be directly related to the material nanomorphology only under a narrow and well-defined range of the measurement conditions.

The PCAFM measurements were carried out on both normal and inverted device architectures. In the normal device geometry, pictured as an inset to Fig. 1a, the OPV layer is spin-coated onto a 45 nm PEDOT:PSS layer on ITO with the film allowed to dry slowly under a petri dish (solvent anneal) to achieve film morphology similar to those reported previously.[2] With a thermally evaporated Ca top contact capped by Ag, the device performance is shown in the main part of Fig. 1a in dark and under nominal AM 1.5G illumination conditions as verified by a calibrated silicon reference cell. The device shows power conversion efficiency (PCE) of 3.9 % without correction for the calibration mismatch factor, estimated to lower the PCE by ≈ 30 %.[17] The inverted device geometry is shown in the inset of figure 1b. We replaced the PEDOT:PSS film with a thin layer (≈ 40 nm) of TiO_2 formed by spin coating followed by a 400 °C annealing step from a sol gel formulation.[18] The use of TiO_2 on ITO as an electron selective contact has been demonstrated previously.[19] The *I-V* characteristics of this device with Au top contacts and the bias applied to the ITO electrode with respect to the top contact, just as in the normal geometry, is plotted in Fig.1b. The characteristics are consistent with an inverted solar cell behavior, demonstrating negative

open circuit voltage, V_{oc}, and positive short circuit current density, J_{sc}. The device efficiency is lower at 1.5 %, mostly due to the reduced V_{oc} and fill factor (FF), which we attribute to the lack of electron blocking layer (such as PEDOT:PSS) under the Au contact and the high resistivity of TiO_2.

The PCAFM measurements performed on the OPV film under illumination at the short circuit conditions in the normal and inverted geometry are shown in Fig. 2a and Fig. 2b, respectively. In this case, the AFM tip replaces the top contact. For these figures, we have overlaid the photocurrent response onto the 3D topography of the active layer, where the red color represents little or no current and green and blue colors represent high photocurrent response. The measurements reveal extreme heterogeneity of the photoresponse. In Fig. 2a, the PCAFM map measured with a moderate work function conductive diamond coated (CDC) tip shows local hot spots of photoresponse corresponding to photogenerated electron current from PCBM regions at the top surface,[12] while the majority of the surface area displays very low current. This is caused by the enrichment of the top interface by P3HT as confirmed by near-edge x-ray absorption fine structure (NEXAFS) spectra of the free surface of identically processed films[9] and recent x-ray photoemission spectroscopy studies.[8] In the inverted geometry, holes are collected at the top surface and, since the surface is mostly enriched by P3HT, the majority of the surface should show high photoresponse, but of the opposite current sign. This is confirmed by the map in Fig. 2b, where we employed a high work function Pt coated AFM tip to collect the hole current from the surface. The percentage of the area displaying high positive photocurrent in inverted device (≈ 80 %) is very similar to the area of low current in the normal device in Fig. 2a. Therefore, the inhomogeneous photoresponse is caused by the surface composition consisting of a P3HT-rich matrix with embedded PCBM regions that appear to range from tens to hundreds of nanometers in size and also hundreds of nanometers apart. This surface composition does not represent the true nanoscale bulk morphology of this system. The phase segregation on the order of hundreds of

nanometers is much larger than the exciton diffusion length in these organic systems (e.g. the exciton diffusion length is on the order of 20 nm or less[20]); given these length scales, one cannot expect to observe quantum efficiencies as high as 60 %[2] and a well-quenched photoluminescence spectrum.[21] Furthermore, the latest electron tomography results[5,6] demonstrate a well-blended morphology in the bulk for the solvent or heat annealed films, consistent with the device performance. Hence, the PCAFM measurements only reveal the morphology of the top surface, which is indirectly related to the bulk three-dimensional morphology.

Having established the material composition at the top interface, we can analyze the bias dependent measurements with the AFM tip and the effect of the tip/sample contact. In general, it is well known that the top metal contact can significantly impact the overall device performance, with the observed trends in normal OPV devices showing a reduction in the short circuit current, $I_{sc,}$ V_{oc} and the FF with an increase of the work function of the contact.[22,23] The choice of the conductive AFM tip can strongly influence the results.

The local *I-V* curves (Fig. 3) look qualitatively different from those observed in macroscopic devices in Fig 1a and 1b. Figure 3a shows the *I-V* data measured by the CDC tip on the film in the normal geometry, with negative voltage corresponding to the reverse bias. In the dark, the typical *I-V* data at all locations on the film surface show a leaky diode-like behavior. Under illumination, the sign of I_{sc} and V_{oc} corresponds to electron collection from the tip under short circuit conditions. Although the FF is low (≈ 12 %), the V_{oc} ranging from 0.3 V to 0.4 V is similar to devices with Ag or Al contacts.[22] At mediocre (low photocurrent) hot spots, the *I-V* response shows a nonlinear increase of current with voltage under the reverse bias, or counter-diode behavior. At very bright hot spots, the FF is larger (≈ 25 %), and the current increases linearly under the reverse bias or, in some cases, shows signs of saturation. In the forward bias, *I-V* curves in both light and dark are similar and appear to be limited by the series resistance. If we utilize a Pt coated tip (Fig. 3b) instead of the CDC tip,

the photocurrent response at 0 V falls below the detection capabilities of our system, and no significant V_{oc} is detected.

For inverted devices (Figs. 3c and 3d), we observe hole collection from the tip under the short circuit conditions (opposite sign of voltage and current) both with both the CDC and the Pt tips. However, the Pt tip shows higher photocurrent and improved FF in the second quadrant compared to the CDC data, indicating that Pt coated tips are better suited for hole collection. For both data sets, the dark *I*-*V*s show significant leakage and counter-diode response in the reverse bias (positive voltages).

We attempt to understand the qualitative features of the *I*-*V* response using a drift-diffusion model of carrier transport. This approach can describe bulk devices well.[24] We are interested in identifying possible physical ingredients that lead to the highly nonideal *I*-*V* characteristics measured with the conductive AFM. In particular, we attempt to provide a quantitative model that reproduces the reverse bias turn-on under illumination seen in the normal device geometry. Figure 4a shows the large energy barrier, $\tilde{\phi}_h$, for hole injection from the AFM tip to the OPV. In order to exhibit nonlinear current response in reverse bias, this energy barrier must decrease with a negative applied bias.

We describe the model and its results briefly here, and refer the reader to Appendix A for more details. We assume a uniform built-in and applied electric field, and neglect recombination and determine the current-voltage relation analytically. To model the reverse bias turn-on under illumination, we posit the existence of localized trap states near the AFM tip that become occupied with negative charge upon photoexcitation (illumination) (we assume a uniform charge density ρ over a distance L_ρ from the tip/OPV interface). Such states have been proposed in previous models of photoconductive gain.[25-27] The presence of trap states may be motivated physically by the interaction of the AFM tip with the OPV. This

interaction may lead to shifts of energy levels of molecules around the tip such that they are separated in energy from nearby states, and hence serve as localized "traps".

The different terms in the electrostatic potential V in Eq. A.3 in Appendix A are shown in Fig. 4a, where V_{app} is the potential due to the applied voltage, V_{photo} is the photo-induced electrostatic potential, V_{bi} is the build-in potential and V_{tot} is the total electrostatic potential in the device. We make the ansatz that the field enhancement at the interface due to this space charge modifies the effective barrier for electron and hole injection, by shifting the effective barrier by an amount $V\ z = L_\rho\ - V\ z = 0$. By letting the space charge potential modify the effective barrier (i.e., modify the boundary condition of the drift-diffusion equation), we assume that the space charge mostly affects the transport process from the metal to the organic material (as opposed to transport within the organic material itself), so that its effect applies near $z = 0$.

Fig. 4b shows a more schematic depiction of our model. It can be understood simply as taking the effective barrier for electron and hole injection to be the value of the total potential a distance L_ρ from the tip/OPV interface. Analysis of this model, given in the Appendix, shows that these charged trap states lead to *I-V* behavior that is qualitatively similar to that seen experimentally.

Figure 5 shows representative dark and illuminated *I-V* curves, calculated with the described framework. We find that the model can capture the reverse bias turn-on behavior. Additionally, a similar treatment of the inverted device geometry does not show reverse bias turn-on, consistent with experiment. However we find that this simple model is unable to describe this behavior with physically reasonable parameters; we need either an unphysically large charge density ρ or a large L_ρ (which is inconsistent with the assumptions of the model), to obtain substantial reverse bias turn on. This implies that the description of reverse bias turn on requires more sophisticated models. In particular, device geometry and

dimensionality likely play a qualitatively important role, as previous models of the AFM tip geometry have shown.[28] Moreover; the modulation of the charge injection process from metal to organic material by the presence of space charge and applied electric field is likely too complicated to be captured by the simple ansatz described above.

In general case, the photoconductive AFM under bias measures both the collection of the photogenerated carriers and the charge injection into p- and n- networks. The interplay between these two effects is illustrated by the complex photoconductive AFM maps presented in Figs. 6a-c. Figure 6a shows the overlaid photocurrent data and topography under short circuit illumination conditions (V_{bias} = 0 V) for a normal-geometry device obtained by the CDC tip. The typical hot spots of photocurrent in yellow and green are observed corresponding to electron collection from PCBM crystallites near the surface within a polymer-rich top surface (red). As a bias voltage of –0.3 V (Fig. 6b) is applied to the ITO with respect to the tip, the red polymer regions start to show photoconductivity, while the hot spots continue to show even more current. At an applied voltage of –1 V, the entire surface becomes practically conductive (Fig. 6c). Since hole injection is essentially a similar concept to electron collection, the sign of the current remains negative. A similar picture applies to the inverted device photocurrent maps under various bias conditions. Therefore, our data shows that assignment of chemical origin of materials based on the photocurrent maps of different contrast under an applied bias may not be reliable.

In summary, we have combined the photoconductive AFM measurement with different AFM tips and two distinct sample architectures to investigate the top surface morphology of blended organic semiconductors based on P3HT and PCBM. Our results point out to enrichment of the top surface with mostly P3HT. We also investigated the local current-voltage characteristics of these samples which we find to be highly nonideal. We attempt to explain the origin of this nonideality with a simple physical model that can reproduce the transport data based on a drift-diffusion model incorporating trapped charges

and interface states at the sample/AFM tip contact; however we find that more sophisticated modeling is likely necessary for a self-consistent description of the data Our findings demonstrate that local photoconductive measurements can be directly related to the material morphology in OPV only under well-defined and well-understood measurement conditions.

Experimental

For preparation of the OPV films on normal device structures, a 1:1 blend of P3HT to PCBM was dissolved in 1,2 dichlorobenzene (DCB) for a total concentration of 30 mg mL^{-1}, heated and stirred at 69 °C overnight. The ITO-coated glass substrate was thoroughly cleaned in hot solvents (first acetone, then isopropyl alcohol), followed by a 10 min ultra-violet ozone treatment, upon which 45 nm of Poly(3,4- ethylenedioxythiophene) poly(styrenesulfonate) (PEDOT:PSS) was spun cast and heat treated in air for 15 min at 120 °C . The active layer ink was spun coated on top of the as-prepared substrate at 500 2π rad/min for 60 s, covered with a petri dish and allowed to slowly dry. For inverted devices, a solution of titanium isopropoxide, prepared by a previously published method,[18] was spun cast on ITO-coated glass at 2000 2π rad/min for 60 s, followed by a high temperature anneal at 400 °C on a hot plate for 1 h to remove organic residue and improve electrical performance of the film. The OPV layer was then spun-cast onto TiO_2 coated ITO in the exact manner described above. For complete device testing, 40 nm of Ca followed by 100 nm of Ag was thermally evaporated onto OPV films for normal devices, and 40 nm of Au was thermally deposited onto OPV layer for inverted devices. For the PCAFM measurement, the excitation source is a 100 mW, 532 nm laser and is directed with a multi-mode optical fiber to illuminate the device from below through the ITO side, while the tip is aligned to the illumination spot from the top. Estimated laser power levels at the sample are ≈ 2 W cm^{-2}. All measurements were performed inside a chamber under continuous nitrogen flow. No significant degradation of photocurrent was observed under the time span of the measurements (up to 30 min).

Acknowledgements
The authors would like to thank Lee Richter for useful discussions. This work has been made possible with the tools and staff support of the nanofabrication research facility at the Center for Nanoscale Science and Technology.

Appendix A

To model this system, we describe the charge transport with (dimensionless) drift-diffusion equations (prime denotes spatial derivative):

$$\begin{aligned} j_n &= En + n' \\ j_p &= Ep - p' \end{aligned} \qquad \text{A.1}$$

$$j_n' = -j_p' = G \qquad \text{A.2}$$

The dimensionless generation rate G is related to the dimensional generation rate $\tilde{G}$ by $\tilde{G} = G\ NDx_0^{-2}$, where N is the characteristic density, D is the diffusion constant, and x_0 is the Debye length, given by $\left(\frac{\epsilon k_B T}{q^2 N}\right)^{1/2}$. Here ϵ is the effective dielectric constant of the organic material, q is the electric charge, and T is the temperature (assumed 300 K). We assume a uniform electric field E, given by $E = \frac{V_{bi} + V_{app}}{L}$, where V_{app} is the applied voltage and V_{bi} is the built-in electric potential, resulting from the difference in work functions of the electrodes. The voltage V is scaled by the thermal voltage $q/k_B T$. We neglect recombination, and with these simplifying assumptions, the current-voltage relation can be written explicitly:

$$\begin{aligned} J\ V_a\ = GL\left(1 + \frac{2}{V_{app} + V_{bi}}\right) + \ p_L + n_R\ \left(\frac{V_{app} + V_{bi}}{L}\right) + \\ \frac{2GL + \ V_{app} + V_{bi}\quad n_R + p_L - n_L - p_R}{e^{V_{app} + V_{bi}} - 1} \end{aligned} \qquad \text{A.3}$$

L is sample thickness, and $n_{L/R}, p_{L/R}$ are electron and hole concentrations at the Left/Right boundaries, determined by the choice of boundary conditions, which we discuss below.

Before discussing the treatment of boundary conditions, we emphasize that our interest is in the reverse-bias turn on of current in illuminated devices in the normal geometry.

To reproduce this feature, we posit the existence of photo-induced charged occupying trapped states near the AFM tip, as described in the main text. We hypothesize that this space charge leads to an applied bias-dependent barrier at the AFM interface, as we describe in more detail below. We also emphasize that in ascribing the effect of the charge induced potential to the boundary condition (and not the potential appearing in the bulk drift-diffusion equation), we are assuming that this potential mostly affects charge transport from metal to organic material (as opposed to transport only within the organic layer itself).

At the right edge (assumed to be the OPV-bulk contact interface), standard boundary conditions apply (we assume infinite recombination velocity):

$$n_R = exp\left[-\frac{E_g}{2}+\phi_R\right], \qquad p_R = exp\left[-\frac{E_g}{2}-\phi_R\right]. \qquad \text{A.4}$$

where ϕ_R is the difference in right contact work function and the electron affinity of the OPV layer, and E_g is the energy difference between the highest occupied molecular orbital of the PCBM and the lowest unoccupied molecular orbital of the P3HT.

At the left edge (the OPV/AFM tip interface), we assume the space charge changes the effective barrier ϕ_L as follows: We take the density of photo-occupied trap states ρ to be spatially constant over some length L_ρ from the tip-OPV interface. For simplicity we adopt a 1D model, and suppose the metallic tip is wide enough so that we may use the method of images to calculate the photo-induced electrostatic potential V_{photo}. This yields $V_{\text{photo}} = -\frac{\rho}{2\epsilon}\ z - L_\rho\ ^2$ for $z < L_\rho$, $V_{\text{photo}} = 0$ for $z > L_{\text{photo}}$. The total electrostatic potential is then given by:

$$V(z) = \frac{z}{L}\left(V_{\mathrm{bi}} + V_{\mathrm{app}} - \frac{\rho L_\rho^2}{2\epsilon}\right) - \frac{\rho}{2\epsilon}(z - L_\rho)^2 + \frac{\rho L_\rho^2}{2\epsilon} \quad \text{for } 0 < z < L_\rho$$
$$V(z) = \frac{z}{L}\left(V_{\mathrm{bi}} + V_{\mathrm{app}} - \frac{\rho L_\rho^2}{2\epsilon}\right) + \frac{\rho L_\rho^2}{2\epsilon} \quad \text{for } L_\rho < z < L, \qquad \text{A.5}$$

where L is the thickness of the OPV layer. The different terms in Eq. A.5 are shown in Fig. 4a. We next make the ansatz that the effective barrier for electron or hole injection is changed by the photogenerated space charge and the associated electric field. We take this effective barrier shift to be given by the potential evaluated at the distance L_ρ from the contact. This choice is slightly artificial, and is only justified if L_ρ is sufficiently small. We nevertheless explore the model as it represents the simplest way to incorporate the effect of (negatively charged) phonogenerated space charge as enhancing the barrier for injection of negative charge (electrons), and decreasing the barrier for injection of positive charge (holes).

Fig. 4a shows how the potential barrier for hole injection is decreased by a negative applied bias. Fig. 4b shows a more schematic depiction of our model. It can be understood simply as taking the effective barrier for electron and hole injection to be the value of the total potential a distance L_ρ from AFM/OPV interface. This prescription leads to a modified boundary condition:

$$n_L = \exp\left[-\frac{E_g}{2} + \tilde{\phi}_L\right],$$
$$p_L = exp\left[-\frac{E_g}{2} - \tilde{\phi}_L\right]. \qquad \text{A.6}$$

where the effective barrier at the left is determined by $V(L_\rho)$, given by:

$$\tilde{\phi}_h = \phi_h - \frac{L_\rho}{L}\left(V_{\mathrm{bi}} + V_{\mathrm{app}}\right) - \frac{\rho L_\rho^2}{2\varepsilon}\left(1 - \frac{L_\rho}{L}\right)$$
$$\tilde{\phi}_e = \phi_e + \frac{L_\rho}{L}\left(V_{\mathrm{bi}} + V_{\mathrm{app}}\right) + \frac{\rho L_\rho^2}{2\varepsilon}\left(1 - \frac{L_\rho}{L}\right) \qquad \text{A.7}$$

In the above, ϕ_L is the difference in AFM work function and the electron affinity of the OPV layer, in the absence of the space charge (for $\rho = 0$).

Fig. 5 shows the resulting *I*-*V* curves, with parameter values given in the caption. We find that we are unable to use physically reasonable parameters to obtain a substantial reverse bias turn on. In the data shown, the value of L_ρ / L is 0.4, which is unrealistically high given the assumptions of the model. We can use a smaller value of L_ρ / L, but to attain reverse bias turn on then requires an unphysically large trap charge density much greater than $10^{19}\,\mathrm{cm}^{-3}$. We therefore conclude that the physics underlying the reverse bias turn-on requires more sophisticated modeling.

REFERENCES

[1] G. Li, Y. Yao, H. Yang, V. Shrotriya, G. Yang, and Y. Yang, Adv. Funct. Mater. 17, 1636 (2007).

[2] G. Li, V. Shrotriya, J. Huang, Y. Yao, T. Moriarty, K. Emery, and Y. Yang, Nat. Mater. 4, 864 (2005).

[3] W. Ma, C. Yang, X. Gong, K. Lee, and A. J. Heeger, Adv. Funct. Mater. 15, 1617 (2005).

[4] X. Yang, J. Loos, S. C. Veenstra, W. J. H. Verhees, M. M. Wienk, J. M. Kroon, M. A. J. Michels, and R. A. J. Janssen, Nano. Lett. 5, 579 (2005).

[5] S. S. van Bavel, E. Sourty, G. de With, and J. Loos, Nano. Lett. 9, 507 (2009).

[6] S. S. van Bavel, E. Sourty, G. de With, K. Frolic, and J. Loos, Macromolecules 42, 7396 (2009).

[7] M. Campoy-Quiles, T. Ferenczi, T. Agostinelli, P. G. Etchegoin, Y. Kim, T. D. Anthopoulos, P. N. Stavrinou, D. D. C. Bradley, and J. Nelson, Nature. Mater. 7, 158 (2008).

[8] Z. Xu, L-M. Chen, G. Yang, C-H. Huang, J. Hou, Y. Wu, G. Li, C-S. Hsu, and Y. Yang, Adv. Funct. Mater. 19, 1 (2009).

[9] D. S. Germack, C. K. Chan, B. H. Hamadani, L. J. Richter, D. A. Fischer, D. J. Gundlach, and D. M. DeLongchamp, Appl. Phys. Lett. 94, 233303 (2009).

[10] D. C. Coffey, O. G. Reid, D. B. Rodovsky, G. P. Bartholomew, and D. S. Ginger, Nano Lett. 7, 738 (2007).

[11] L. S. C. Pingree, O. G. Reid, and D. S. Ginger, Nano Lett. 9, 2946 (2009).

[12] B. H. Hamadani, S. Jung, P. M. Haney, L. J. Richter, and N. B. Zhitenev, Nano Lett. 10, 1611 (2010).

[13] H. Xin, O. G. Reid, G. Ren, F. S. Kim, D. S. Ginger, S. A. Jenekhe, ACS Nano, 4, 1861 (2010).

[14] X-D. Dang, A. B. Tamayo, J. Seo, C. V. Hoven, B. Walker, T-Q. Nguyen, Adv. Funct. Mater. (2010).

[15] A. Alexeev, J. Loos, and M. M. Koetse, Ultramic. 106, 191 (2006).

[16] M. Dante, J. Peet, and T-Q. Nguyen, J. Phys. Chem. C. 112, 7241 (2008).

[17] V. Shrotriya, G. Li, Y. Yao, T. Moriarty, K. Emery, and Y. Yang, Adv. Funct. Mater. 16, 2016 (2006).

[18] N. Gergel-Hackett, B. H. Hamadani, B. Dunlap, J. Suehle, C. Richter, C. Hacker, and D. Gundlach, IEEE. Elect. Dev. Lett. 30, 706 (2009).

[19] C. Waldauf, M. Morana, P. Denk, P. Schilinsky, K. Coakley, S. A. Choulis, and C. J. Brabec, Appl. Phys. Lett. 89, 233517 (2006).

[20] K. M. Coakley, M. D. McGehee, Appl. Phys. Lett. 83, 3380 (2003).

[21] M. Drees, H. Hoppe, C. Winder, H. Neugebauer, N. S. Sariciftci, W. Schwinger, F. Schäffler, C. Topf, M. C. Scharber, Z. Zhu, and R. Gaudiana, J. Mater. Chem. 15, 5158 (2005).

[22] M. O. Reese, M. S. White, G. Rumbles, D. S. Ginley, and S. E. Shaheen, Appl. Phys. Lett. 92, 053307 (2008).

[23] V. D. Mihailetchi, L. J. A. Koster, P. W. M. Blom, Appl. Phys. Lett. *85*, 970 (2004).

[24] L. J. A. Koster, E. C. P. Smits, V. D. Mihailetchi, P. W. M. Blom, Phys. Rev. B 72, 085205 (2005).

[25] E. Ahlswede, J. Hanisch, and M. Powalla, Appl. Phys. Lett. 90, 063513 (2007).

[26] D. Gupta, S. Mukhopadhyay, K. S. Narayan, Sol. Energy Mater. Sol. Cells. (2008).

[27] H-Y. Chen, M. K. F. Lo, G. Yang, H. G. Monbouquette, and Y. Yang, Nature. Nano. 3, 543 (2008).

[28] O. G. Reid, K. Munechika, and D. S. Ginger, Nano Lett. 8, 1602 (2008).

Figure Captions

FIG. 1: (a) Typical *J-V* characteristics of 1:1 P3HT:PCBM solar cells in the normal device geometry where holes are collected from the PEDOT/ITO and electrons from Ca/Ag interfaces. (b) The *J-V* characteristics for a similarly prepared OPV film in an inverted device architecture. With the bias applied exactly to the same electrodes (ITO vs top contact), we see an inverted device performance.

FIG. 2: 3-D plot of the film topography overlaid with the photocurrent map collected simultaneously under short circuit illumination conditions for (a) normal device geometry with a conductive diamond-coated AFM tip and (b) inverted geometry with a Pt coated AFM tip.

FIG. 3: Local dark and light *I-V* measurements with the (a) CDC tip on the normal device, (b) Pt-coated tip on the normal device, (c) CDC tip on the inverted device and (d) Pt-coated tip on the inverted device. Each *I-V* curve is averaged over data from several spots.

FIG. 4: (a) The details of the potential profile near the tip/OPV interface leading to light-assisted injection under reverse bias conditions for the normal device. (b) A more schematic depiction of our model showing that the effective barrier for hole injection can be taken as the value of the total potential a distance L_ρ from the tip/OPV interface.

FIG. 5: Calculated *J-V* plots in dark and under light for the normal device, based on the physical model of drift and diffusion described here and in more detail in the Appendix. Parameters used:
$E_g = 1\text{eV},\ \phi_L = -0.1\ \text{eV},\ \phi_R = -0.4\ \text{eV},\ L = 300x_0,\quad \rho/\text{Coulomb} = 10^{17}\,\text{cm}^{-3},\ L_\rho/L = 0.4,\ G = 10^{-7}$
Here $\phi_{L/R}$ are measured from mid-gap, and J_0 is defined as $J_0 = qDN/x_0$.

FIG. 6: 3-D plot of the film topography with the overlaid photocurrent map for a normal device geometry as a function of the reverse bias voltage: (a) 0 V (b) –0.3 V (c) –1 V. Under bias, initial non-photoconductive regions start to show significant conductance as seen in the *I-V* data of Fig. 3a, corresponding to hole injection from the tip into polymer-rich regions.

Figure 1, Hamadani, Phys Rev B

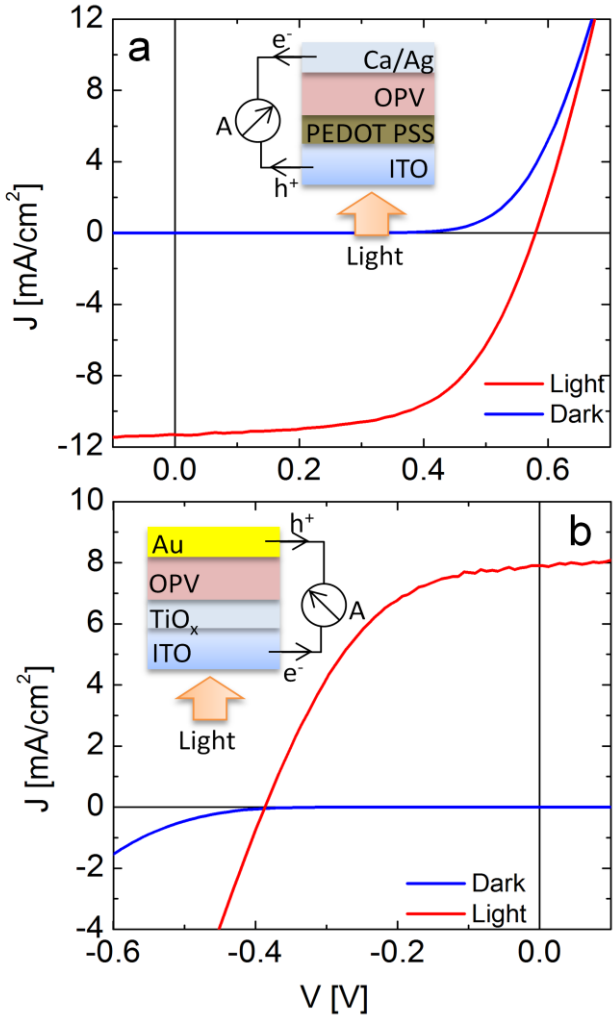

Figure 2, Hamadani, Phys Rev B

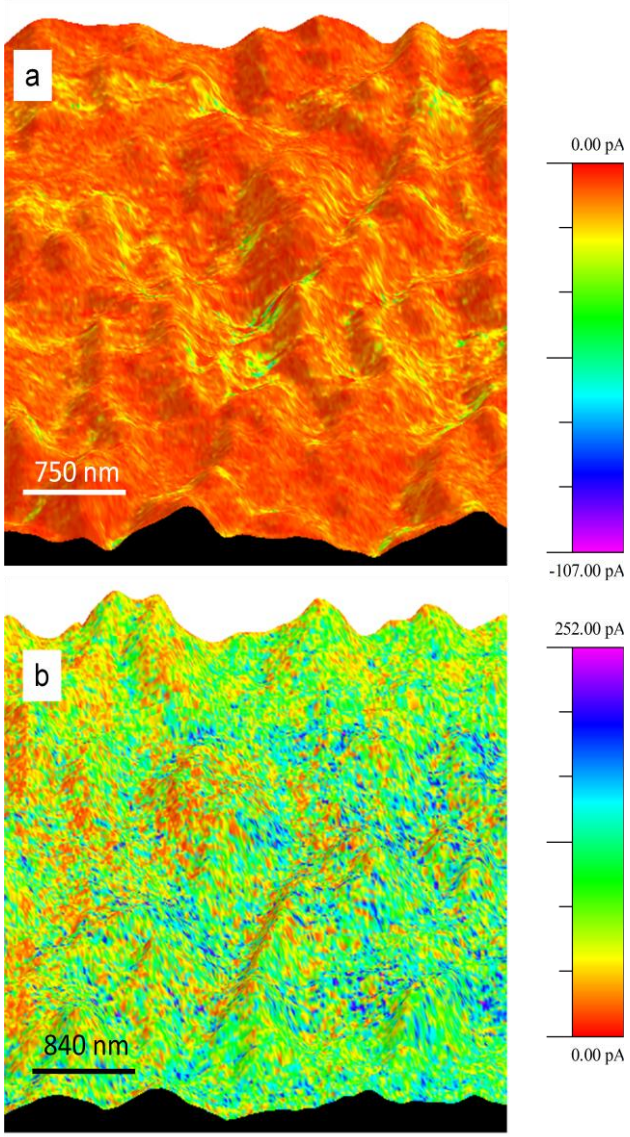

Figure 3, Hamadani, Phys Rev B

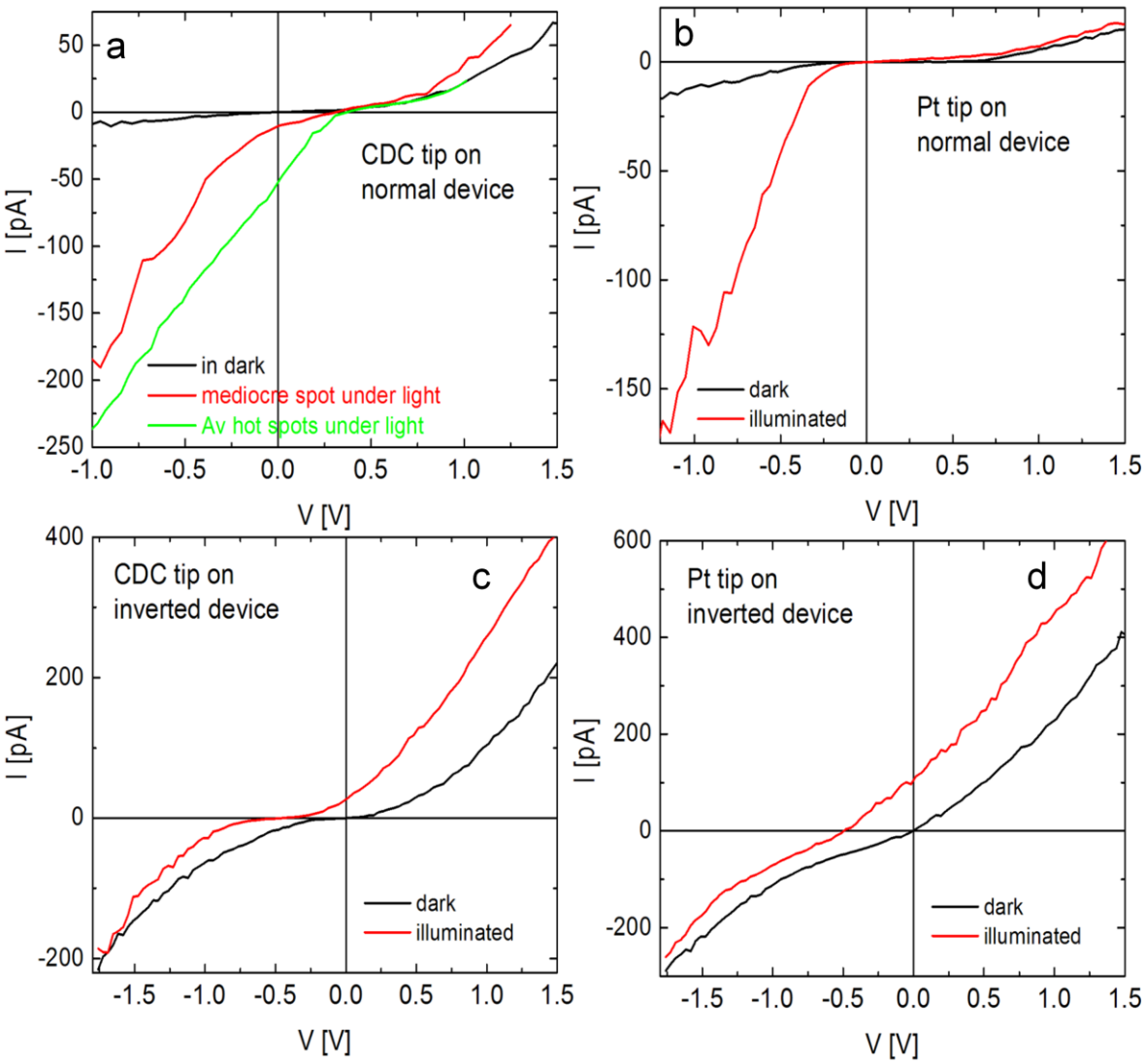

Figure 4, Hamadani, Phys Rev B

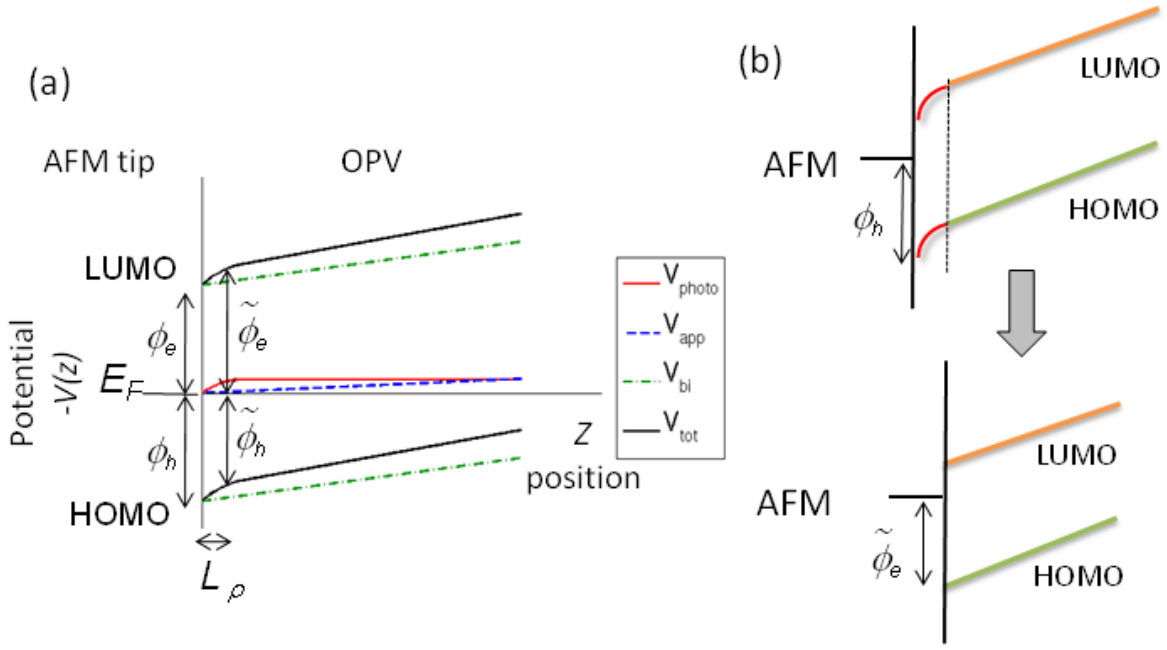

Figure 5, Hamadani, Phys Rev B

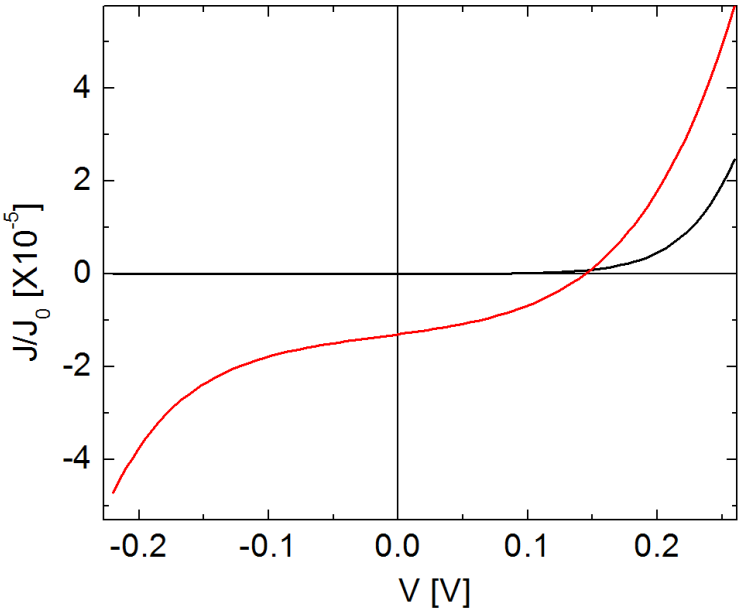

Figure 6, Hamadani, Phys Rev B